Elucidating the Nature of the Active Phase in Copper/Ceria Catalysts for CO Oxidation

Joseph S. Elias,[†] Nongnuch Artrith,[§] Matthieu Bugnet,[‡] Livia Giordano,[#§] Gianluigi A. Botton,[‡] Alexie M. Kolpak,[§] and Yang Shao-Horn*[ΔO§]

[†]Department of Chemistry, Massachusetts Institute of Technology, Cambridge, Massachusetts 02139, United States

[§]Department of Mechanical Engineering, Massachusetts Institute of Technology, Cambridge, Massachusetts 02139, United States

[Δ]Research Laboratory of Electronics, Massachusetts Institute of Technology, Cambridge, Massachusetts 02139, United States

[O]Department of Materials Science and Engineering, Massachusetts Institute of Technology, Cambridge, Massachusetts 02139, United States

[‡]Department of Materials Science and Engineering, McMaster University, Hamilton, Ontario L8S 4L7, Canada

[#]Dipartimento di Scienza dei Materiali, Università di Milano-Bicocca, Via R. Cozzi 53, 20125 Milan, Italy

* Corresponding Author e-mail: shaohorn@mit.edu

Table of Contents:

Experimental Methods

General experimental considerations

All reagents were obtained from commercial vendors and were used without further purification. All reactions were performed under ambient conditions unless otherwise noted. The precursor compounds **Cu^{II}-3-MeO-salpn**, **Ce^{III}-3-MeO-salpn** and **Cu^{II}-Ce^{III}-3-MeO-salpn** were prepared according to our previous report.[1]

General procedure for the preparation of single-phase $Cu_yCe_{1-y}O_{2-x}$ nanoparticles

Single-phase nanoparticles with the stoichiometry $Cu_yCe_{1-y}O_{2-x}$ for y = 1, 3, 8% were prepared according to our previous report.[1] Appropriate amounts, not exceeding 1.0 mmol total, of the parent **Ce^{III}-3-MeO-salpn** and **Cu^{II}-Ce^{III}-3-MeO-salpn** complexes were heated with magnetic stirring in 40 mL oleylamine at 180 °C under an Ar flow for 4 hours in a three-neck flask equipped with a reflux condenser and bump trap. The resulting dark brown solutions were divided into eight 5 mL fractions, flocculated with ethanol (40 mL each) and the flocculant was isolated by centrifugation (7100 rpm for 15 min). The flocculant was then redissolved in hexanes (5 mL each) and bulk precipitates were removed by centrifugation (5000 rpm for 1 min) and decanting of the dark brown hexanes solutions. This process was repeated once to give dark-brown hexanes solutions of phase-pure $Cu_yCe_{1-y}O_{2-x}$.

To remove the organic capping layer for catalysis and further characterization, as-prepared solutions of $Cu_yCe_{1-y}O_{2-x}$ were dropcast into alumina crucibles and annealed at 400 °C in synthetic air for 4 hrs to give phase-pure, free-flowing powders of $Cu_yCe_{1-y}O_{2-x}$.

Synthesis of $Cu_{0.01}Ce_{0.99}O_{2-x}$ nanoparticles

$Cu_{0.01}Ce_{0.99}O_{2-x}$ was prepared from the pyrolysis of **Ce^{III}-3-MeO-salpn** (0.633 g, 0.947 mmol) and **Cu^{II}-Ce^{III}-3-MeO-salpn** (0.038 g, 0.052 mmol) in 40 mL oleylamine (*vide supra*) to give $Cu_{0.01}Ce_{0.99}O_{2-x}$ as a pale khaki powder after annealing (0.091 g, 0.53 mmol, 53%).

Synthesis of $Cu_{0.03}Ce_{0.97}O_{2-x}$ nanoparticles

$Cu_{0.03}Ce_{0.97}O_{2-x}$ was prepared from the pyrolysis of **Ce^{III}-3-MeO-salpn** (0.501 g, 0.749 mmol) and **Cu^{II}-Ce^{III}-3-MeO-salpn** (0.183 g, 0.250 mmol) in 40 mL oleylamine (*vide supra*) to give $Cu_{0.03}Ce_{0.97}O_{2-x}$ as a khaki powder after annealing (0.040 g, 0.24 mmol, 24%).

Synthesis of $Cu_{0.08}Ce_{0.92}O_{2-x}$ nanoparticles

$Cu_{0.08}Ce_{0.92}O_{2-x}$ was prepared from the pyrolysis of **Ce^{III}-3-MeO-salpn** (0.223 g, 0.333 mmol) and **Cu^{II}-Ce^{III}-3-MeO-salpn** (0.487 g, 0.667 mmol) in 40 mL oleylamine (*vide supra*) to give $Cu_{0.08}Ce_{0.92}O_{2-x}$ as a dark khaki powder after annealing (0.127 g, 0.675 mmol, 76.5%).

General procedure for the preparation of $CuO/Cu_yCe_{1-y}O_{2-x}$

Mixed-phase CuO/Cu$_y$Ce$_{1-y}$O$_{2-x}$ materials were prepared under conditions similar to the preparation of single-phase Cu$_y$Ce$_{1-y}$O$_{2-x}$ described above with notable differences; the reaction was carried out in air and with excess **Cu^{II}-3-MeO-salpn** precursor. Appropriate amounts of **Cu^{II}-Ce^{III}-3-MeO-salpn** and **Cu^{II}-3-MeO-salpn** were heated with magnetic stirring in 40 mL oleylamine at 180 °C in air for 4 hours in a three-neck flask equipped with a reflux condenser and bump trap. The resulting dark-brown solutions were worked up with ethanol and hexanes as described above for Cu$_y$Ce$_{1-y}$O$_{2-x}$, dropcast into alumina crucibles, and annealed in air at 400 °C for 4 hours to give free-flowing powders of CuO/Cu$_y$Ce$_{1-y}$O$_{2-x}$.

Synthesis of CuO/Cu$_{0.05}$Ce$_{0.95}$O$_{2-x}$ nanoparticles

CuO/Cu$_{0.05}$Ce$_{0.95}$O$_{2-x}$ was prepared from the pyrolysis of **Cu^{II}-3-MeO-salpn** (0.807 g, 2.00 mmol) and **Cu^{II}-Ce^{III}-3-MeO-salpn** (0.730 g, 1.00 mmol) in 40 mL oleylamine (*vide supra*) to give CuO/Cu$_{0.05}$Ce$_{0.95}$O$_{2-x}$ as an olive powder after annealing (0.119 g).

Synthesis of CuO/Cu$_{0.08}$Ce$_{0.92}$O$_{2-x}$ nanoparticles

CuO/Cu$_{0.08}$Ce$_{0.92}$O$_{2-x}$ was prepared from the pyrolysis of **Cu^{II}-3-MeO-salpn** (0.332 g, 0.822 mmol) and **Cu^{II}-Ce^{III}-3-MeO-salpn** (0.730 g, 1.00 mmol) in 40 mL oleylamine (*vide supra*) to give CuO/Cu$_{0.08}$Ce$_{0.92}$O$_{2-x}$ as an olive powder after annealing (0.050 g).

Synthesis of CuO/Cu$_{0.09}$Ce$_{0.91}$O$_{2-x}$ nanoparticles

CuO/Cu$_{0.09}$Ce$_{0.91}$O$_{2-x}$ was prepared from the pyrolysis of **Cu^{II}-3-MeO-salpn** (0.167 g, 0.413 mmol) and **Cu^{II}-Ce^{III}-3-MeO-salpn** (0.730 g, 1.00 mmol) in 40 mL oleylamine (*vide supra*) to give CuO/Cu$_{0.09}$Ce$_{0.91}$O$_{2-x}$ as an olive powder after annealing (0.078 g).

Powder X-ray diffraction (PXRD)

Powder X-ray diffraction patterns were collected on a PANalytical X'Pert PRO diffractometer using Bragg-Brentano geometry and nickel-filtered Cu-K$_\alpha$ radiation (λ = 1.54056 Å). Samples were prepared using 0.2 mm deep zero-background sample wells composed of boron-doped, *p*-type silicon from MTI Corporation. Powder profiles were fit with pseudo-Voigt functions using the FullProf suite.[2] In each case, the crystallite sizes (*d*) of the Cu$_y$Ce$_{1-y}$O$_{2-x}$ phase were estimated using the Scherrer equation to the fitted (220) peak assuming a shape factor *K* of 0.94 for spherical crystallites of cubic symmetry, after accounting for instrumental line broadening. The crystallite sizes thus obtained were used to estimate the turnover frequencies assuming surface segregation of copper sites (*vide infra*).

Transmission electron microscopy (TEM)

Samples studied by transmission electron microscopy were prepared by dropcasting dilute ethanol suspensions of annealed (CuO)/Cu$_y$Ce$_{1-y}$O$_{2-x}$ onto lacey carbon gold TEM grids. Bright field images were acquired at 200 keV using a low-background beryllium sample holder on a JEOL 2010-FEG transmission electron microscope at MIT, which is equipped with a field-emission electron gun and an ultra-high resolution pole piece, resulting in a point-to-point

resolution of 1.9 Å. Fast Fourier transforms (FFTs) were implemented using the ImageJ software.[3] For the acquisition of bright-field images, care was taken to prevent beam-induced reconstruction of individual nanocrystals by minimizing the duration of beam exposure. Energy dispersive X-ray spectroscopy (EDS) was performed in scanning transmission mode using a 1 nm diameter electron beam. Quantification was carried out by using a simple ratio technique in INCA (Oxford Instruments), which accounts for X-ray absorption and thickness effects. Nevertheless, the thickness parameter used in quantification was varied to determine if the inconsistent apparent thicknesses of the samples shown in Figure S3 contribute to the inconsistencies in the copper quantification. For all samples measured, we saw no significant change in copper content, suggesting that X-ray absorption is minimal in these samples. Copper substitution was quantified for the $Cu_yCe_{1-y}O_{2-x}$ phase only by judicious choice of probe position; CuO phases were avoided by differentiating them by image contrast.

Electron Energy Loss Spectroscopy

$Cu_{0.1}Ce_{0.9}O_{2-x}$ and $Mn_{0.1}Ce_{0.9}O_{2-x}$ samples were prepared by diluting annealed nanoparticle powders in HPLC grade methanol, ultrasonicating, and dropcasting onto Si_3N_4 window grids (Norcada Inc.). Experiments were carried out on a FEI Titan cubed (80-300) (S)TEM at McMaster University, equipped with aberration correctors of the probe and image forming lenses and a high resolution GIF Quantum spectrometer. The microscope was operated at 80 kV in STEM mode, and the spectrum images were recorded with a collection angle of ~55 mrad, and a current below 40 pA to minimize beam damage.

Raman Spectroscopy

Raman spectra were acquired at room temperature on a LabRAM HR800 microscope (Horiba Jobin Yvon) using an external 17 mW HeNe 632.8 nm laser (Melles Griot) focused with a 50× objective lens and a 25% filter. A silicon substrate was used to calibrate the Raman shift. The sampling time and range were identical for all spectra (100-1000 cm^{-1}, 5 × 10 s) using a 600 mm^{-1} grating.

X-ray absorption spectroscopy (XAS)

X-ray absorption measurements at the copper K-edge were performed at the bending magnet station X11A of the National Synchrotron Light Source (NSLS) at Brookhaven National Laboratory.[4] The electron storage ring operated at 2.8 GeV with a stored current in the range of 200 – 300 mA. The excitation energies were selected with a double crystal monochromator (Si-(111)), which was detuned by 40% to suppress higher harmonics. The incident and transmitted beams were monitored using ionization chambers equilibrated with appropriate mixtures of nitrogen and argon gas. The energy calibration of the monochromator was set by calibrating the inflection point of the absorption spectrum of transition-metal foils to their literature values.[5]

Copper K-edge spectra were acquired in fluorescence yield (FY) mode using a resistively-heated *in-situ* catalyst furnace equipped with a 5-grid Lytle fluorescence detector[6] (both from the EXAFS Company). For FY measurements, the signal passed through a silver Soller slit assembly prior to detection by the ionization chamber, which had a continuous flow of Ar. The pellet for *in-situ* studies was prepared by first sieving $Cu_{0.08}Ce_{0.92}O_{2-x}$ (10.5 wt%), boron

nitride (75.5 wt%) and high-surface area Vulcan XC-72 carbon (14 wt%, Cabot) to 400 mesh followed by thorough mixing and grinding with an agate mortar and pestle. A 50 mg pellet (5 mm x 12 mm) was pressed and introduced into the catalyst furnace, the window of which was sealed with Kapton tape. Gas mixtures (CO and O_2 balanced in He) were flowed through the catalyst pellet by means of mass-flow controllers at flow-rates of 50 mL min^{-1}. The pellet was slowly heated to 300 °C under lean conditions (0.01 atm CO and 0.025 atm O_2 at a flow rate of 50 mL min^{-1}) and gases were allowed to equilibrate for 15 minutes before the acquisition of XAFS spectra.

Absorption spectra were normalized using the Autobk algorithm found in the IFEFFIT program[7] of the Horae XAFS analysis suite.[8] First, a linear fit of the pre-edge line was subtracted from the spectrum. A fourth-order knot-spline polynomial was used to fit the post-edge line and the edge step was normalized to unity. Prior to Fourier transforms, the EXAFS was multiplied by a Hanning window covering the first and last ~10% of the data range.

Single-point BET surface area determination

Values for the surface areas of annealed $(CuO)/Cu_yCe_{1-y}O_{2-x}$ powders were estimated from single-point BET measurements from desorption of N_2 at room temperature (after adsorption at 77 K in 30% N_2/He) using a ChemBET Pulsar apparatus (Quantachrome). For the calculation of the turnover frequency (TOF) in mixed phase $CuO/Cu_yCe_{1-y}O_{2-x}$ powders, it was assumed in that the measured BET surface area was attributed to the $Cu_yCe_{1-y}O_{2-x}$ phase since the crystallite size is significantly smaller than CuO by TEM and PXRD.

CO oxidation catalysis

CO oxidation kinetic measurements were acquired in a home-made 3.81 mm i.d. quartz plug-flow reactor. For each measurement, the annealed catalyst powder (20 mg) was mixed with 1.705 g oven-dried sand (V_{bed} = 1.086 cm^3) and was then loaded into center of the reactor, filling the remaining volume with sand. The temperature of the catalyst was recorded using a K-type thermocouple inserted into the catalyst bed. The compositions of the feed and down-stream gases were recorded by on-line gas chromatography (Agilent 490 supplied with a molecular sieve COX column and a thermal conductivity reactor), recording every 5 °C. The percent conversion was calculated according to

$$\% \text{ Conversion} = \frac{p_{CO_2}}{p_{CO} + p_{CO_2}} \cdot 100\%$$

where p_{CO2} and p_{CO}, the partial pressures of CO_2 and CO, respectively, are determined directly from the relative peak area of the CO_2 and CO peaks normalized to the internal He standard. Prior to and following each catalytic test, the flow rate of the gas upstream was measured directly with a bubble flowmeter, and the percent conversion below 12.5% was converted to mass-normalized rates of CO oxidation (in units of μmol CO s^{-1}g$_{cat}^{-1}$) for the Arrhenius plots according to

$$r_{mass} = \frac{\frac{\% \text{ Conversion}}{100} \cdot r_{CO} \cdot 1000}{V_m \cdot 60 \cdot m_{cat}}$$

$$= \frac{\% \text{ Conversion} \cdot r_{CO}}{6 \cdot V_m \cdot m_{cat}}$$

where r_{CO} is the volumetric flow rate of CO of the feed stream (in mL min^{-1}), V_m is the molar volume of a gas (from the ideal gas law, $V_m = RT/p$, in mol/L) and m_{cat} is the mass of the loaded catalyst in grams. The specific (area-normalized) rates for CO oxidation (in units of mol CO s^{-1}m$_{cat}^{-2}$) were thus calculated according to

$$r_{area} = \frac{r_{mass}}{A_S} \cdot 10^{-6}$$

where A_s is the surface area of the catalyst (in m^{2}g^{-1}) as measured by BET (*vide supra*). Finally, the turnover frequency (*TOF*) as reported in Figure 2B was estimated according to the formula

$$TOF \approx \frac{r_{area} \cdot N_A}{PD_{111} \cdot y}$$

where N_A is Avogadro's number, PD_{111} is the planar density of cerium atoms in the {111} plane of CeO$_2$ (in units of atoms m^{-2}) and y is the amount of copper ions substituted into the Cu$_y$Ce$_{1-y}$O$_{2-x}$ phase as determined by STEM-EDS. The planar density of the {111} facet was used in the calculation of the *TOF* because (a) it was found by HRTEM to be the most predominant crystallographic termination in individual Cu$_y$Ce$_{1-y}$O$_{2-x}$ nanoparticles (the other being {100}),[1] and (b) PD_{111} is only 15.5% larger than PD_{100} (7.89*10^{18} Ce m^{-2} and 6.83*10^{18} Ce m^{-2}, respectively), and hence likely *underestimates* the actual TOF.

   This calculation assumes homogeneous copper substitution into the CeO$_2$ lattice and, according to the discussion in the main text, is thus likely *overestimating* the actual TOF because copper segregates to the surface. To take surface segregation into account, we can estimate a correction factor to the TOF reported above based on the geometry and crystal structure of a representative nanoparticle

$$\frac{n_{Cu, \, homogeneous}}{n_{Cu, \, surface \, segregation}} = \frac{A_{S,np} \cdot PD_{111} \cdot \cancel{y}}{V_{np} \cdot \left(\frac{Z}{V_{cell}}\right) \cdot \cancel{y}}$$

where $n_{Cu, \, surface \, segregation}$ is the number of copper sites that segregate to the surface, which, for our purposes, we assume to be all of the copper sites in the nanoparticle. $n_{Cu, \, homogeneous}$ is the total number of copper sites at the surface of an individual nanoparticle assuming that copper is distributed evenly within the ceria lattice. Here, V_{np} and $A_{S,np}$ are the volume and surface area of the nanoparticle, respectively, and Z is the number of cerium atoms in the unit cell of CeO$_2$ (which has a volume of V_{cell}). In the case of Cu$_y$Ce$_{1-y}$O$_{2-x}$, we have established that the crystal habit is a truncated octahedron, which has a known volume and surface area:

$$\frac{n_{Cu,\,homogeneous}}{n_{Cu,\,surface\,segregation}} = \frac{(6 + 12\sqrt{3})a^2 \cdot PD_{111}}{8\sqrt{2}a^3 \cdot \left(\frac{Z}{V_{cell}}\right)}$$

$$= \frac{(6 + 12\sqrt{3}) \cdot PD_{111}}{8\sqrt{2}a \cdot \left(\frac{Z}{V_{cell}}\right)}$$

where a is the edge length of the truncated octahedron. In our previous study, we found the diameter of annealed $Cu_{0.08}Ce_{0.92}O_{2-x}$ to be 36 Å from Scherrer analysis of the X-ray powder diffraction patterns,[1] which is consistent with our HRTEM results here. If we define the diameter of a truncated octahedron as $3a$, and use crystallographic parameters for CeO_2 ($Z = 4$, $V_{cell} = 158.46$ Å^3), this correction is ~0.62, which is within the scatter of the kinetic measurements summarized in Figure 2B. Nevertheless, these corrections are tabulated in Table S3 and are used as the basis for the estimation of the turnover frequencies (assuming *surface segregation* of copper sites) summarized in Figure S5. Although the turnover frequencies for the catalysts studied here do decrease assuming surface segregation of copper sites, this decrease is systematic. The turnover frequencies for the different catalysts are identical within the scatter of the measurement, consistent with Figure 2 and the conclusion of the main text.

Computational Methods

DFT+U slab studies of {111}-terminated $Cu_2Ce_{34}O_{72-x}$

Plane-wave basis set spin-polarized DFT+U calculations were executed employing the exchange and correlation energy functional expressed in the Perdew-Burk-Ernzerhof (PBE) generalized gradient approximation (GGA)[9-12] using projector-augmented wave (PAW) pseudopotentials.[13,14] All calculations were performed within the Vienna Ab Initio Simulation Package (VASP) suite[15-18,14] using either the Cray XE6 ("Hopper") or Cray XC30 ("Edison") supercomputers at the National Energy Research Scientific Computing Center (NERSC).

A 3x3x4 hexagonal slab model of the CeO_2 (111) surface ($Ce_{36}O_{72}$) was used as the starting point for models of the $Cu_yCe_{1-y}O_{2-x}$ catalyst, separated by 15 Å of vacuum to prevent interactions between slabs. To simulate copper substitution, two copper atoms were placed in cerium vacancies ($Cu_{Ce}^{\times}$ in Kröger-Vink notation) in the parent $Ce_{36}O_{72}$ slab to give the aliovalent, copper-substituted models of stoichiometry $Cu_2Ce_{34}O_{72}$. As described in the text, three configurations were considered to study the relative thermodynamic stability of copper segregation and agglomeration (Figure 4A inset). In the solid solution (ss-) models, copper atoms replace cerium atoms in the first and third CeO_2 layers (Ce-Ce interatomic distance = 12.859 Å). In the nearest-neighbor (nn-) models, copper atoms replace nearest-neighbor cerium atoms on the first CeO_2 layer of the slab (Ce-Ce interatomic distance = 3.877 Å), and in the next-nearest-neighbor (nnn-) model, copper atoms replace next-nearest-neighbor cerium atoms on the first CeO_2 layer (Ce-Ce interatomic distance = 6.715 Å). To simulate aliovalent substitution of the copper ions (Cu^{3+}, Cu^{2+}, and Cu^+, or $Cu_{Ce}^{'}$, $Cu_{Ce}^{''}$, and $Cu_{Ce}^{'''}$ in Kröger-Vink notation), an appropriate number of oxygen atoms were removed in the vicinity of the transition-metal centers for charge compensation; the removal of a single oxygen atom corresponds to the reduction of

each copper atom by 1 electron. For example, removal of a single oxygen atom from $Cu_2Ce_{34}O_{72}$ to give $Cu_2Ce_{34}O_{71}$ suggests that each of the copper atoms in the slab has been reduced by one electron from Cu^{4+} to Cu^{3+}. Hence, these models are denoted as $Cu^{(4-x)+}_2Ce_{34}O_{72-x}$, where x refers to the number of charge-compensating oxygen atoms removed (the oxygen non-stoichiometry). For all nn-$Cu_2Ce_{34}O_{72-x}$ structures, as well as ss-$Cu^{4+}_2Ce_{34}O_{72}$, ss-$Cu^{3+}_2Ce_{34}O_{71}$, nnn-$Cu^{4+}_2Ce_{34}O_{72}$ and nnn-$Cu^{3+}_2Ce_{34}O_{71}$ surfaces, reduction at the copper (as opposed to surrounding cerium atoms) was confirmed by inspecting the net magnetization for each atom of the slab and examination of the partial density of states. Interestingly, for the ss-$Cu^{2+}_2Ce_{34}O_{70}$ slab, copper reduction was accompanied by reduction of the cerium atoms surrounding the oxygen vacancy.

The (111) surface of CeO_2 was chosen on the basis of HRTEM analysis both here and in earlier studies, which indicate that the (111) is the predominant surface exposed in truncated octahedral $Cu_yCe_{1-y}O_{2-x}$ crystallites.[1] The choice of a 3x3x4 slab with substitution of two copper atoms was also rationalized in terms of experimental data; these models give 5.6% Cu substitution in CeO_2 while we have found here that y in $Cu_yCe_{1-y}O_{2-x}$ can vary between 1 and 9% Cu (*vide supra*). A 3x3x4 slab was also chosen in order to simulate varying degrees of substitutional homogeneity (*i.e.* the ss-, nn-, and nnn- models mentioned above).

A Hubbard U_{eff} ($U_{eff} = U - J$) correction term of 4.0 eV acting on the $4f$ orbitals of cerium was included in all calculations to allow for a more accurate description of the electronic structure of both oxidized and reduced ceria, which has been discussed previously.[19] The inclusion of a Hubbard U_{eff} term acting on the copper $3d$ orbitals may perturb the energies of oxygen formation in the model slabs and hence the thermodynamic preference of one oxidation state over the other.[19] We found that the introduction of a Hubbard U_{eff} term on the copper $3d$ states did not perturb the relative values of ΔG_F for the slabs studied here. Only after applying values for U_{eff} in excess of 4.0 eV did we see any changes in the ordering of ΔG_F vs. μ_O plots, hence we set U_{eff} to 0.0 eV for copper $3d$ states for all studies on $Cu^{(4-x)+}_2Ce_{34}O_{72-x}$.

To correct for any systematic errors arising from the periodic boundary conditions with the asymmetric slabs studied here, a linear electrostatic potential (*i.e.* a dipole correction) was applied to the local potential. Electronic and ionic optimization of the slabs was carried out using the conjugate gradient algorithm employing a plane-wave cutoff of 400 eV. All atomic layers were allowed to relax until all the forces acting on the atoms reached a value below 0.01 eV Å^{-1}. Owing to the large size of the slabs studied here, all data were reported from the integration of the Brillouin zone at the Γ point only. We found that the slab energies calculated at the Γ point varied by less than 35 meV from those calculated using a 2x2x1 Monkhorst-Pack mesh, which justifies our choice of integration at the Γ point only.

Estimates for the Gibbs energy of formation (ΔG_F) of the different slabs of $Cu^{(4-x)+}_2Ce_{34}O_{72-x}$ as a function of oxygen partial pressure were determined according to a strategy previously reported by Reuter, *et al.*[20] ΔG_F was determined relative to a reference structure (ss-$Cu_2Ce_{34}O_{72}$) by taking into account the formation of oxygen vacancies:

$$\Delta G_{F,x} = G(Cu_2Ce_{34}O_{72\text{-}x}) - G(ss\text{-}Cu_2Ce_{34}O_{72}) + x\mu_O(p,T)$$

If changes in entropy of the solid phases are neglected,[20] we can express ΔG_F in terms of energy (E) calculated by DFT:

$$\Delta G_{F,x} = E(Cu_2Ce_{34}O_{72\text{-}x}) - E(ss\text{-}Cu_2Ce_{34}O_{72}) + x\mu_O(p,T)$$

where the chemical potential for oxygen (μ_O) is

$$\mu_O(p,T) = \mu_O(p_0,T) + \frac{1}{2}k_B T \ln\frac{p}{p_0}$$

The standard chemical potential for oxygen at $p_0 = 1$ atm ($\mu_O(p_0,T)$) is found from thermodynamic tables. The value for $\mu_O(p,T)$ is referenced with respect to the total energy of an oxygen atom in a molecule of O_2 as calculated by DFT. The temperature used in these calculations (700 K where $\mu_O(p_0,T) = -0.73$ eV)[20] was chosen to roughly correspond to the temperature at which $Cu_yCe_{1-y}O_{2-x}$ samples were annealed.

Nanoparticle model for Monte-Carlo simulations

To allow a direct comparison with experiment, we devised an atomistic nanoparticle model based on the experimentally observed Wulff shape with a {111} to {100} surface ratio of 3:1. The relative areas of the two crystal faces as function of their relative distance from the particle center, $h_{\{111\}}/h_{\{100\}}$, are

$$A_{\{100\}} = 12\left(\sqrt{3}\frac{h_{\{111\}}}{h_{\{100\}}} - 1\right)^2 \text{ and } A_{\{111\}} = 6\sqrt{3} - 8\sqrt{3}\left(\sqrt{3}\frac{h_{\{111\}}}{h_{\{100\}}} - \frac{3}{2}\right)^2 \text{ for } \frac{1}{\sqrt{3}} \leq \frac{h_{\{111\}}}{h_{\{100\}}} \leq \frac{2}{\sqrt{3}},$$

so that $A_{\{111\}}/A_{\{100\}} = 3$ corresponds to $h_{\{111\}}/h_{\{100\}} \approx 0.887$ (see graphical solution in Fig. S1). We used this relationship to build the nanoparticle structure with approximately 3.5 nm diameter and the desired relative surface areas shown in Figs. 3b and 3c.
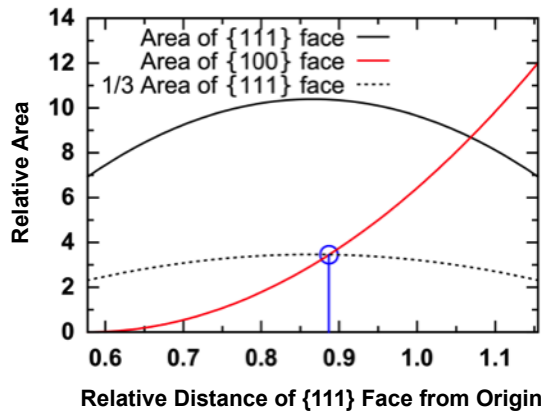
Figure S1. Graphical solution of the surface area ratio as function of the surface distance from the particle center. The solid black and red lines indicate the {111} and {100} surface areas, respectively. The dotted black line corresponds to 1/3 of the {111} surface area, and the blue circle points out the {111}:{100} ratio of 3:1.

Artificial neural network potential for $Cu_yCe_{1-y}O_{2-x}$ nanoparticles

The size of the nanoparticle model and the extensive sampling required to determine the copper distribution throughout the particle prevent the direct application of density functional

theory (DFT). We therefore follow the approach by Behler and Parrinello and employ artificial neural networks (ANNs) for the accurate interpolation of DFT reference calculations.[21,22] An invariant representation of the local atomic environment is achieved by using a basis set of radial and angular functions (Behler *symmetry functions*). The basis parameters employed in this work are given in **Tables S1 and S2**; see previous work for the analytical function definitions.[23] The atomic energy network (ænet) package was used for all simulations with ANN potentials.[24]

Table S1. Parameters of the radial basis function (Behler *symmetry function*) G^2 of reference [23] used for the description of the local atomic structure within a cutoff radius of $R_c = 6.5$ Å.

| No.	Species	η (Å^{-2})	No.	Species	η (Å^{-2})
1	Ce	0.003214	12	Cu	0.124987
2	O	0.003214	13	Ce	0.214264
3	Cu	0.003214	14	O	0.214264
4	Ce	0.035711	15	Cu	0.214264
5	O	0.035711	16	Ce	0.357106
6	Cu	0.035711	17	O	0.357106
7	Ce	0.071421	18	Cu	0.357106
8	O	0.071421	19	Ce	0.714213
9	Cu	0.071421	20	O	0.714213
10	Ce	0.124987	21	Cu	0.714213
11	O	0.124987			

In total, around 1100 $Cu_yCe_{1-y}O_{2-x}$ periodic bulk, surface ({111} and {100}), and isolated cluster structures were used for the construction of the ANN potential. The DFT calculations of these reference structures were carried out using the FHI-aims package[25] using *tight* settings (6th order expansion of the Hartree potential, radial integration grids with 434 points in the outer shell, and a tier 2 basis set). Relativistic effects were included with atomic ZORA.[26] Structural energies were generally converged to 1 meV/atom, and atomic forces to 10 meV/Å. For all calculations the exchange-correlation functional by Perdew, Burke, and Ernzerhof was used.[10]

Around 1000 reference structures were used for the training of the ANN potential, and the accuracy of the interpolation was verified against an independent testing set of around 100 structures that were not used for training. The root mean squared error (RMSE) of the final ANN potential is 6.8 meV/atom for the training set and 8.7 meV/atom for the testing set. The mean absolute errors are 5.4 and 7.1 meV/atom for the training and the testing set, respectively. The ANN potential energies of all structures in the reference set are compared to their DFT references in Fig. S2. We stress that the excellent accuracy of the ANN potential could only be achieved because all reference structures are closely related to the nanoparticle model of the previous section. The ANN potential of this work would not be suitable for the investigation of structurally very different Cu/Ce/O systems.

Table S2 Parameters of the angular basis function (Behler *symmetry function*) G^4 of reference [23] used for the description of the local atomic structure within a cutoff radius of $R_c = 6.5$ Å. Each set of parameters listed in the table corresponds to 6 equivalent functions for the 6 possible combinations of atomic species (Ce-Ce, Ce-O, Ce-Cu, O-O, O-Cu, Cu-Cu) among neighboring atom pairs in the local structural environment of an atom (Ce, O, Cu).

No.	η (Å^{-2})	λ	ζ
22-27	0.000357	1.0	1.0
28-33	0.000357	-1.0	1.0
34-39	0.000357	1.0	4.0
40-45	0.000357	-1.0	4.0
46-51	0.010713	1.0	1.0
52-57	0.010713	-1.0	1.0
58-63	0.010713	1.0	4.0
64-69	0.010713	-1.0	4.0
70-75	0.028569	1.0	1.0
76-81	0.028569	-1.0	1.0
82-87	0.028569	1.0	4.0
88-93	0.028569	-1.0	4.0
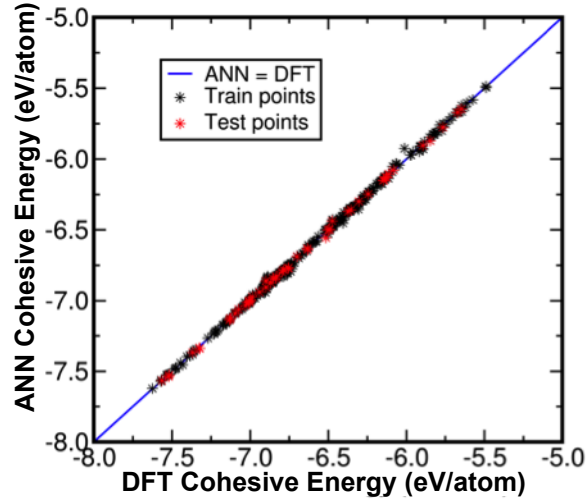
Figure S2. Comparison of the cohesive energies predicted by the ANN potential and their DFT reference values. The diagonal (blue line) corresponds to perfect correlation. The energies of structures from the training and test sets are shown as black and red points, respectively.

Monte-Carlo simulations

The Monte-Carlo (MC) simulations were carried out in the grand canonical ensemble, i.e., the copper grand potential

$$\Phi_{Cu} = E^{ANN} - TS - \mu_{Cu} N_{Cu}$$

was minimized in the simulated annealing runs for a given oxygen vacancy concentration and copper chemical potential, μ_{Cu}. In the above equation, E^{ANN} is the configurational energy

predicted by the ANN potential, T is the temperature, S is the configurational entropy, and N_{Cu} is the number of copper atoms in the nanoparticle.

All MC simulations were repeated at least three times to guarantee reproducibility. The nanoparticle that was analyzed for the article is representative and has a copper concentration closest to the experimentally observed 10%.
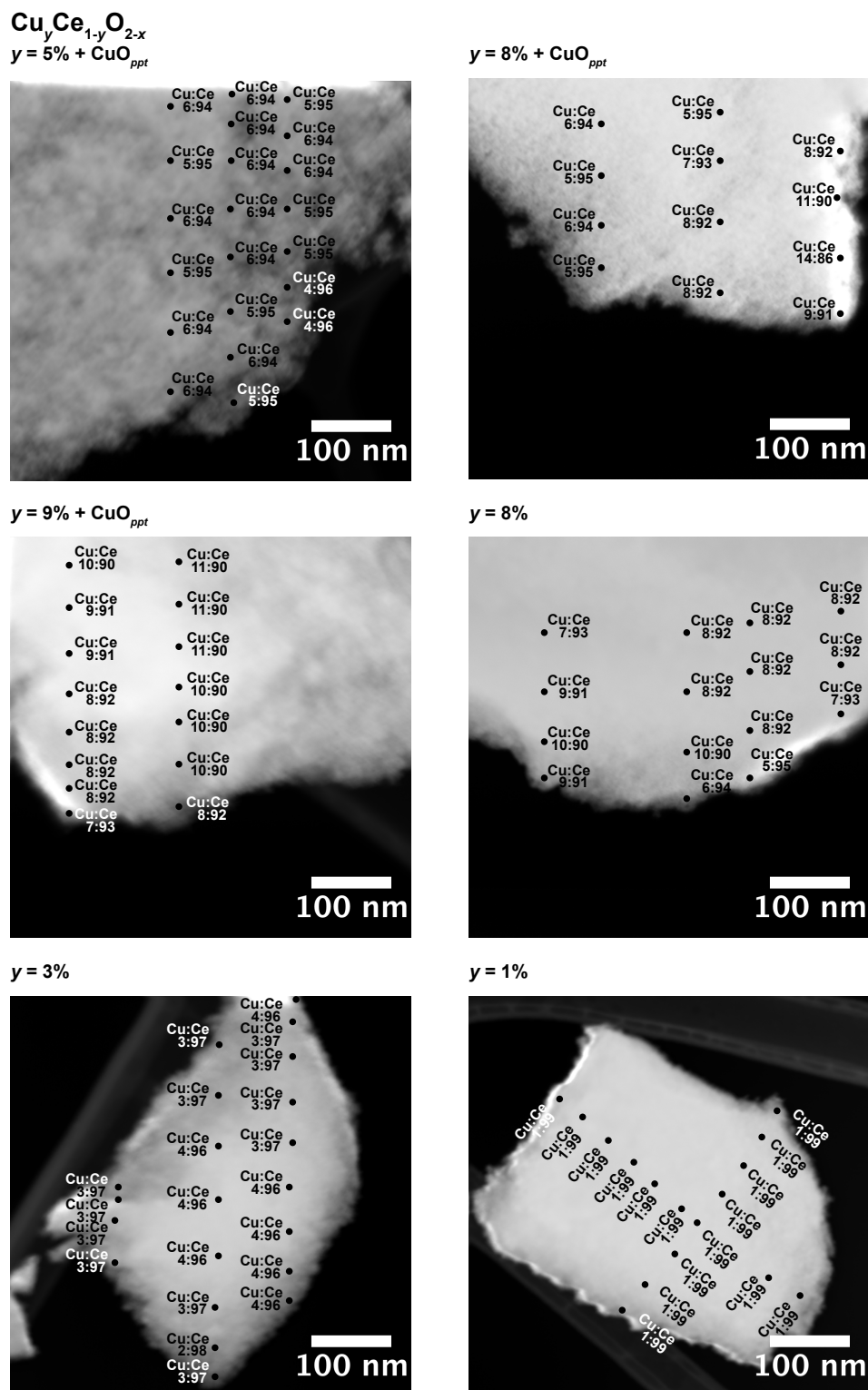
Figure S3. High angle annular dark-field (HAADF) images acquired in STEM mode coupled with X-ray energy dispersive spectroscopy (EDS) of CuO/Cu$_y$Ce$_{1-y}$O$_{2-x}$ catalysts. Mean copper substitution is 5.4(6)%, 8(3)%, 9(1)%, 8(1)%, 3.4(7)% and 1.0(2)%, respectively.
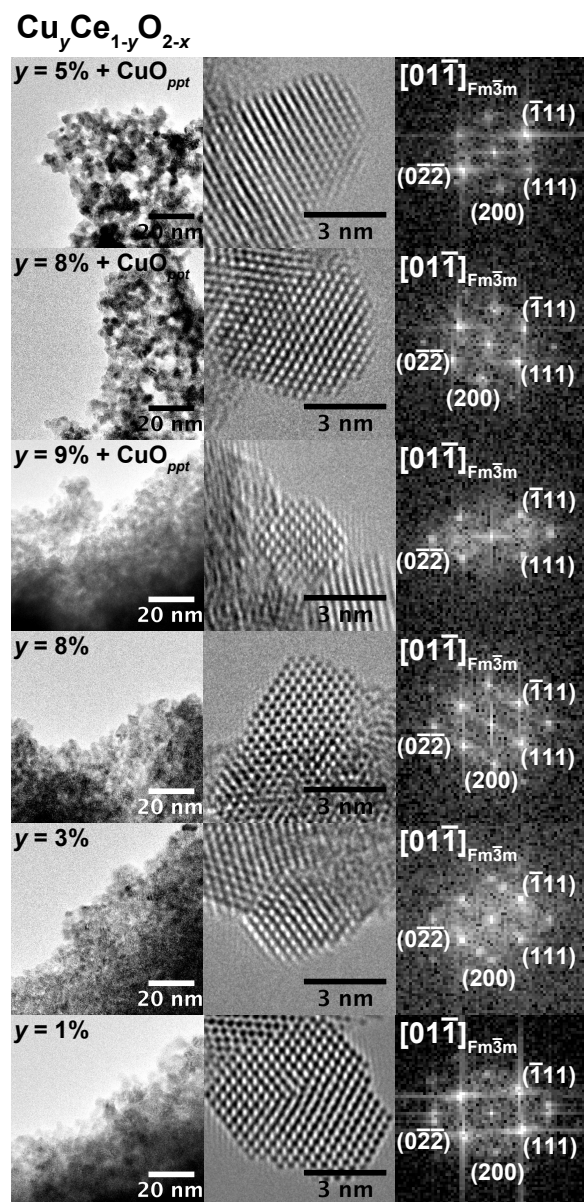
Cu$_y$Ce$_{1-y}$O$_{2-x}$


Figure S4. HRTEM of annealed CuO/Cu$_y$Ce$_{1-y}$O$_{2-x}$ catalysts. Included are low-magnification images (left), high-resolution images of the Cu$_y$Ce$_{1-y}$O$_{2-x}$ phase (center) and their fast Fourier transforms (right).
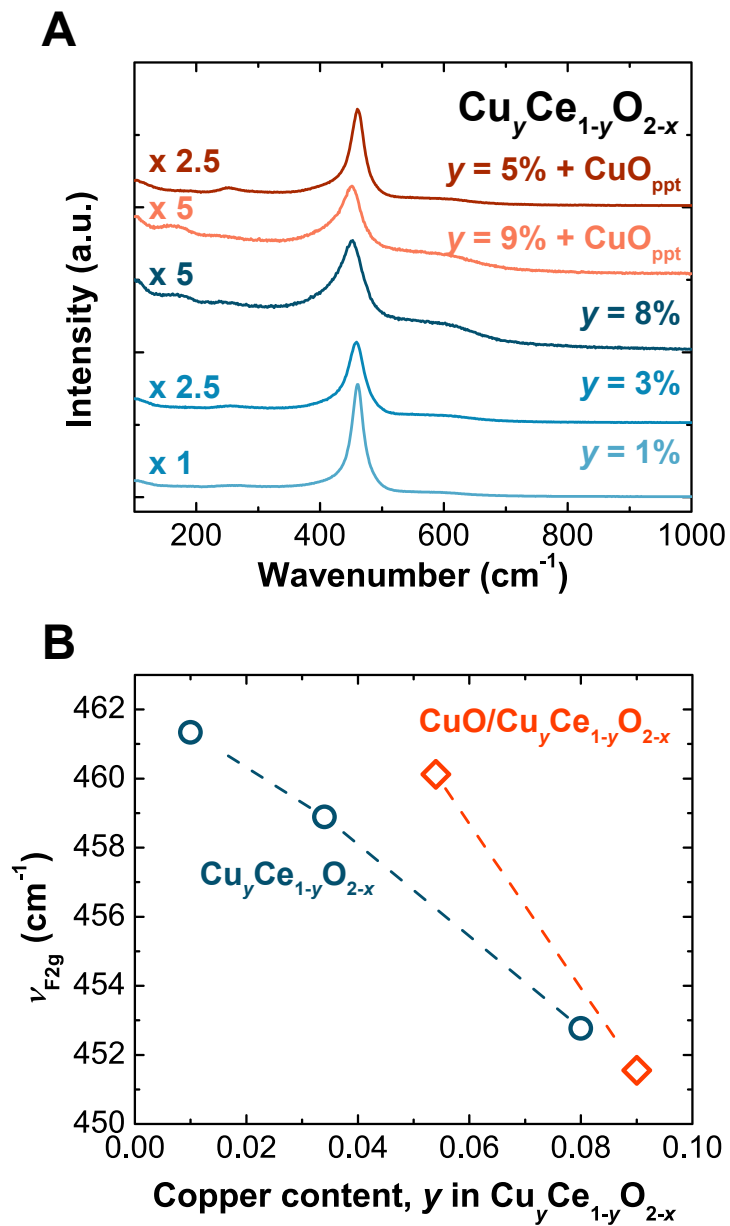
Figure S5. Raman spectra of $Cu_yCe_{1-y}O_{2-x}$ and $CuO/Cu_yCe_{1-y}O_{2-x}$ acquired at room temperature. (A) Raw spectra and (B) measured frequency of the F_{2g} mode as a function of copper substitution in $Cu_yCe_{1-y}O_{2-x}$ (y).
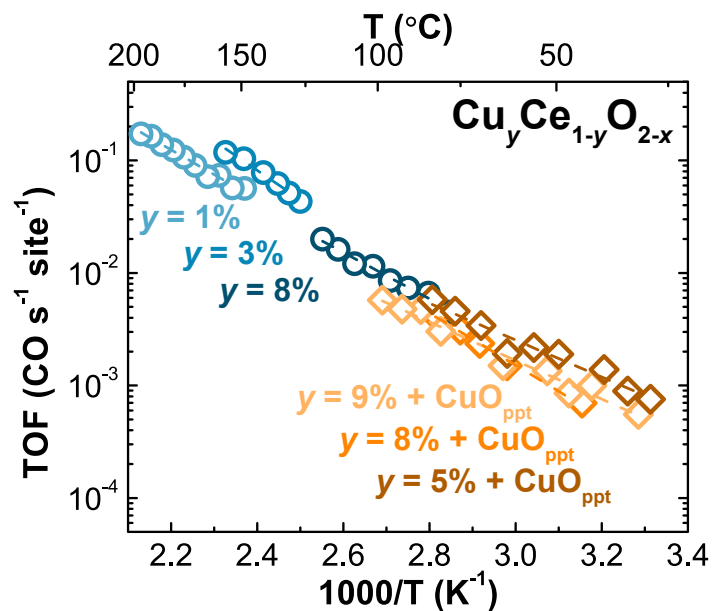
Figure S6. Arrhenius plots for CO oxidation over $CuO/Cu_yCe_{1-y}O_{2-x}$ normalized by surface copper site in $Cu_yCe_{1-y}O_{2-x}$ assuming surface segregation of copper. Rates were measured in 1% CO, 2.5% O_2 balanced in He at a flow rate of 1300 mL min^{-1} g^{-1}.
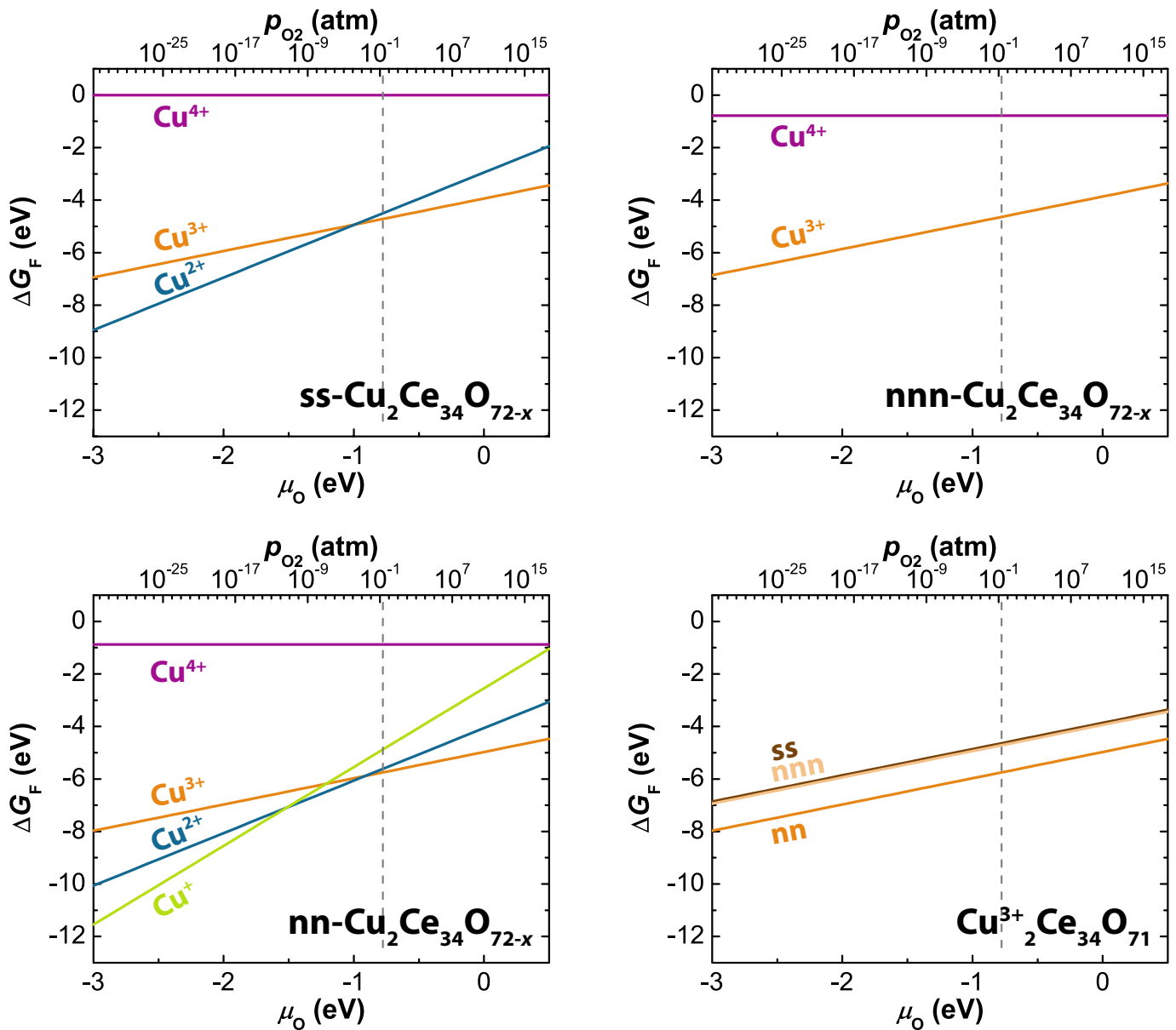
Figure S7. DFT+*U*-calculated phase diagrams for ss-, nnn- and nn-Cu$_2$Ce$_{34}$O$_{72-x}$ slab models computed at 700 K. The dashed grey lines correspond to 0.21 atm O$_2$ (i.e. air). The lowest-energy slabs for each of the three models, corresponding to the stoichiometry Cu$^{3+}_2$Ce$_{34}$O$_{71}$, are also shown for comparison.
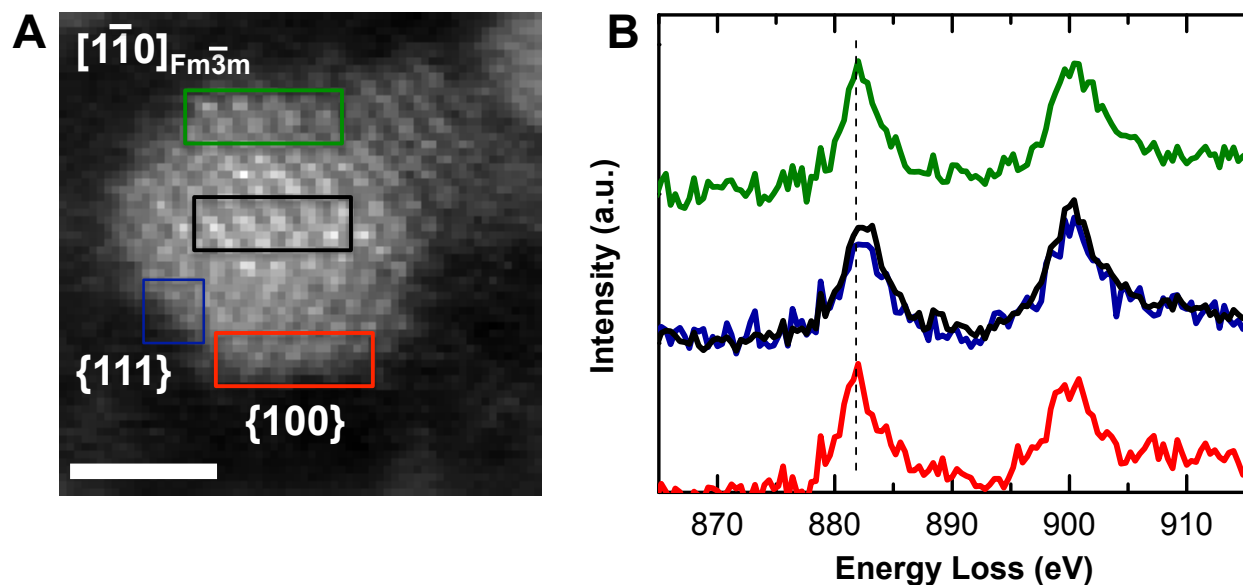
Figure S8. STEM-EELS analysis of an individual $Mn_{0.1}Ce_{0.9}O_{2-x}$ nanoparticle. (A) Dark field image acquired simultaneously with the spectrum images (scale bar: 2 nm), (B) Ce $M_{4,5}$-edge spectra corresponding to the boxed regions in A. The dotted line in B refers to the peak at 882 eV ascribed to Ce^{3+}.

Table S3. Apparent activation energies (E_A) for CO oxidation on $CuO/Cu_yCe_{1-y}O_{2-x}$ powders, their BET surface areas, (A_S) and crystallographic parameters for the $Cu_yCe_{1-y}O_{2-x}$ phase. Standard uncertainties in the last digits are included in parentheses.

Compound	E_A (kJ mol^{-1})	A_S (m^2 g^{-1})	a (Å)	$d_{Scherrer\ (220)}$ (Å)	R factors (%)	χ^2	$n_{homog.}/n_{surf.\ seg.}$	y (EDS)
$CuO/Cu_{0.05}Ce_{0.95}O_{2-x}$	31	114	5.4143(2)	59.0	1.55, 1.97	1.16	0.38	0.054(6)
$CuO/Cu_{0.08}Ce_{0.92}O_{2-x}$	44	119	5.4159(6)	52.0	1.94, 2.66	2.01	0.43	0.08(3)
$CuO/Cu_{0.09}Ce_{0.91}O_{2-x}$	33	78	5.4145(1)	54.7	2.45, 3.19	2.24	0.41	0.09(1)
$Cu_{0.08}Ce_{0.92}O_{2-x}$	40	52	5.420(3)	33.8	2.15, 2.80	1.23	0.66	0.08(1)
$Cu_{0.03}Ce_{0.97}O_{2-x}$	50	17	5.426(4)	36.6	2.25, 2.84	1.28	0.61	0.034(7)
$Cu_{0.01}Ce_{0.99}O_{2-x}$	42	29	5.4156(6)	52.8	2.16, 2.79	1.17	0.42	0.010(2)

Table S4. Crystallographic parameters for the CuO phase in $CuO/Cu_yCe_{1-y}O_{2-x}$ powders. Standard uncertainties in the last digits are included in parentheses.

Compound	a (Å)	b (Å)	c (Å)	β (°)	$d_{Scherrer\ (111)}$ (Å)
$CuO/Cu_{0.05}Ce_{0.95}O_{2-x}$	4.6836(3)	3.4341(3)	5.1338(4)	99.360(4)	274.5
$CuO/Cu_{0.08}Ce_{0.92}O_{2-x}$	4.693(1)	3.435(1)	5.129(2)	99.34(2)	152.1
$CuO/Cu_{0.09}Ce_{0.91}O_{2-x}$	4.646(4)	3.439(2)	5.146(4)	99.31(3)	115.5

References

(1) Elias, J. S.; Risch, M.; Giordano, L.; Mansour, A. N.; Shao-Horn, Y. *J. Am. Chem. Soc.* **2014**, *136*, 17193-17200.

(2) Rodriguez-Carvajal, J. *Commission on Powder Diffraction (IUCr)* **2001**, *26*, 12-19.

(3) Schneider, C. A.; Rasband, W. S.; Eliceiri, K. W. *Nat. Methods* **2012**, *9*, 671-675.

(4) Sayers, D. E.; Heald, S. M.; Pick, M. A.; Budnick, J. I.; Stern, E. A.; Wong, J. *Nuclear Instruments and Methods in Physics Research* **1983**, *208*, 631-635.

(5) Bearden, J. A.; Burr, A. F. *Reviews of Modern Physics* **1967**, *39*, 125-142.

(6) Lytle, F. W.; Greegor, R. B. a. S. D. R.; Marques, E. C.; Wong, J.; Spiro, C. L.; Huffman, G. P.; Huggins, F. E. *Nucl. Instrum. Methods A* **1984**, *226*, 542 - 548.

(7) Newville, M. *J. Synchrotron Radiat.* **2001**, *8*, 322-324.

(8) Ravel, B.; Newville, M. *J. Synchrotron Radiat.* **2005**, *12*, 537-541.

(9) Perdew, J. P.; Burke, K.; Ernzerhof, M. *Phys. Rev. Lett.* **1996**, *77*, 3865-3868.

(10) Perdew, J. P.; Burke, K.; Ernzerhof, M. *Phys. Rev. Lett.* **1997**, *78*, 1396-1396.

(11) Perdew, J. P.; Chevary, J. A.; Vosko, S. H.; Jackson, K. A.; Pederson, M. R.; Singh, D. J.; Fiolhais, C. *Phys. Rev. B: Condens. Matter Mater. Phys.* **1992**, *46*, 6671-6687.

(12) Perdew, J. P.; Chevary, J. A.; Vosko, S. H.; Jackson, K. A.; Pederson, M. R.; Singh, D. J.; Fiolhais, C. *Phys. Rev. B: Condens. Matter Mater. Phys.* **1993**, *48*, 4978-4978.

(13) Bochl, P. E. *Phys. Rev. B: Condens. Matter Mater. Phys.* **1994**, *50*, 17953-17979.

(14) Kresse, G.; Joubert, D. *Phys. Rev. B: Condens. Matter Mater. Phys.* **1999**, *59*, 1758-1775.

(15)   Kresse, G.; Furthmüller, J. *Phys. Rev. B: Condens. Matter Mater. Phys.* **1996**, *54*, 11169-11186.

(16)   Kresse, G.; Furthmüller, J. *Comput. Mater. Sci.* **1996**, *6*, 15-50.

(17)   Kresse, G.; Hafner, J. *Phys. Rev. B: Condens. Matter Mater. Phys.* **1993**, *47*, 558-561.

(18)   Kresse, G.; Hafner, J. *Phys. Rev. B: Condens. Matter Mater. Phys.* **1994**, *49*, 14251-14269.

(19)   Krcha, M. D.; Janik, M. J. *Int. J. Quantum Chem.* **2014**, *114*, 8-13.

(20)   Reuter, K.; Scheffler, M. *Phys. Rev. B: Condens. Matter Mater. Phys.* **2001**, *65*, 035406.

(21)   Behler, J.; Parrinello, M. *Phys. Rev. Lett.* **2007**, *98*, 146401.

(22)   Behler, J. *J. Phys.: Condens. Matter* **2014**, *26*, 183001.

(23)   Behler, J. *J. Chem. Phys.* **2011**, *134*, 074106.

(24)   Artrith, N.; Urban, A. *Comput. Mater. Sci.* **2016**, *114*, 135-150.

(25)   Blum, V.; Gehrke, R.; Hanke, F.; Havu, P.; Havu, V.; Ren, X.; Reuter, K.; Scheffler, M. *Comput. Phys. Commun.* **2009**, *180*, 2175-2196.

(26)   van Lenthe, E.; Baerends, E. J.; Snijders, J. G. *J. Chem. Phys.* **1994**, *101*, 9783-9792.